



PCCP

**Insights into Lithium Ion Deposition on Lithium Metal Surfaces**

Journal:	<i>Physical Chemistry Chemical Physics</i>
Manuscript ID	CP-ART-06-2020-003399.R2
Article Type:	Paper
Date Submitted by the Author:	08-Sep-2020
Complete List of Authors:	Angarita-Gomez, Stefany; Texas A and M University College Station, Chemical Engineering Balbuena, Perla; Texas AandM University, Chemical Engineering

SCHOLARONE™  
Manuscripts

## Insights into Lithium Ion Deposition on Lithium Metal Surfaces

Stefany Angarita-Gomez and Perla B. Balbuena\*  
Department of Chemical Engineering,  
Texas A&M University, College Station, TX 77843  
\*e-mail: [balbuena@tamu.edu](mailto:balbuena@tamu.edu)

### Abstract

Lithium metal is among the most promising anodes for the next generation of batteries due to its high theoretical energy density and high capacity. Challenges such as extreme reactivity and lithium dendrite formation have kept lithium metal anodes away from practical applications. However, the underlying mechanisms of Li ion deposition from the electrolyte solution onto the anode surface are still poorly understood due to their inherent complexity. In this work, density functional theory calculations and thermodynamic integration via constrained molecular dynamics simulations are conducted to study the electron and ion transfer between lithium metal slab and the electrolyte in absence of an external field. We explore the effect of the solvent chemistry and structure, distance of the solvated complex from the surface, anion-cation separation, and concentration of Li-salts on the deposition of lithium ions from the electrolyte phase onto the surface. Ethylene carbonate (EC), 1,2-Dimethoxyethane (DME), 1,3-Dioxolane (DOL), and mixtures of them are used as solvents. These species compete with the salt anion and the Li cation for electron transfer from the surface. It is found that the structure and properties of the solvation shell around the lithium cation has a great influence on the ability of the cation to diffuse as well as on its surrounding electron environment. DME molecules allow easier motion of the lithium ion compared with EC and DOL molecules.

The slow growth approach allows the study of energy barriers for the ion diffusion and desolvation during the deposition pathway. This method helps elucidating the underlying mechanisms on lithium-ion deposition and provides a better understanding of the early stages of Li nucleation.

## Introduction

Lithium metal is considered the 'Holy Grail' anode because of its high theoretical capacity (3860 mAh g<sup>-1</sup>) and negative electrochemical potential (-3.04 V vs standard hydrogen electrode).<sup>1,2</sup> Lithium metal anodes are crucial for next-generation batteries including Lithium-Sulfur and Lithium-air batteries which show high promise for electric vehicles and other energy storage applications.<sup>3-6</sup> However, key factors like poor cyclability as well as the safety issues related to the uneven lithium electrodeposition, dendrite growth, and unstable solid electrolyte interphase (SEI) are keeping lithium metal batteries away from commercialization.<sup>7</sup>

Lithium dendrites damage the battery performance as revealed by the low Coulombic efficiency, capacity fading, and catastrophic short-circuit failures, which are some of the effects detected upon cycling.<sup>8</sup> Uneven dendrite-like growth could crack the SEI exposing fresh lithium that reacts with the electrolyte and consumes active material.<sup>6</sup> Therefore, understanding the lithium deposition mechanisms and their correlation with the interfacial chemistries is important for elucidating and eventually preventing dendrite nucleation and growth.

Various techniques have been implemented for the study of dendrite nucleation and growth. These studies could be divided into two categories: understanding of the

morphology and growth of the dendrite and a second one oriented to the development of potential suppression strategies. For example, *in situ* optical microscopy for direct observation of lithium dendritic growth,<sup>9</sup> synchrotron hard X-ray microtomography has been used to image the structures residing on both sides of the lithium metal/electrolyte interface and to characterize the morphology of dendrite growth during cycling.<sup>10</sup> Several efforts have been done to investigate suppression of the dendrite growth such as the use of high concentrated electrolytes,<sup>11</sup> and more recently localized high-concentration electrolytes<sup>12</sup> that achieve high current rate cycling with high Coulombic efficiency without dendrite growth for hundreds of cycles.<sup>13</sup> Additives to the electrolyte or the use of porous electrode structures that may work as a host of lithium metal are used to improve the uniform electrodeposition of lithium.<sup>14,15</sup> Other approaches used for dendrite suppression include the alteration of operating conditions, which also changes the initial stages of nucleation addressed in this study. Recent research has focused on the effect of the temperature on dendrite growth.<sup>16-18</sup> A homogeneous increase of temperature could promote Li-ion diffusion on the electrolyte phase as well as self-diffusion once the ion is deposited and reduced.<sup>19-21</sup>

Various theories and models have been used to investigate the electrodeposition and develop a systematic way to determine the lithium cation deposition mechanisms. Theories like the Bartone-Bockris surface-tension model,<sup>22</sup> Brownian statistical simulation model,<sup>23</sup> Chazalviel electromigration limited model<sup>24</sup> and interesting growth theories such as that proposed by Yamaki and collaborators have been used for this purpose.<sup>25</sup> Although these models have provided additional insights, no agreement or perfect model has been found yet. The main difference among these models is on the preferential

growth location of the next deposition in the early stage of dendrite formation.<sup>26</sup> With respect to this point, a recent ab initio-based model showed that the initial nucleation would be ruled more by kinetics than by thermodynamics factors and demonstrated the basis for inhomogeneous growth.<sup>27</sup> Analytical and computational models based on the mechanical properties of the dendrite are also proposed for the understanding of the dendrite growth.<sup>28-30</sup>

In this work, density functional theory (DFT) and ab initio molecular dynamics (AIMD) along with constrained molecular dynamics are used to understand the electrodeposition of lithium cation on lithium metal anodes. Charge transfer, electron distribution, and structural changes are studied in various settings that emulate the early stages of cation deposition. Several electrolytes, salt concentrations, solvated complex-surface and cation-anion distances are analyzed to gain insights into the effect of these variables on ion deposition mechanisms. Constrained molecular dynamics simulations are performed using the Blue Moon ensemble<sup>31</sup> to calculate diffusion and deposition pathways and barriers. The Blue Moon ensemble method allows evaluating the free energy profile along a reaction coordinate direction. The advantage of the technique is that it facilitates the detection of one or more barriers that would not likely be crossed in regular molecular dynamics simulations.<sup>31,32</sup>

### **Computational and system details**

Calculations were performed using the Vienna ab Initio Simulation Package (VASP).<sup>33-35</sup> Electron-ion interactions were described by the projector augmented wave (PAW) pseudopotentials<sup>36,37</sup> provided in VASP database. The Perdew-Burke-Ernzerhof generalized gradient approximation (GGA-PBE)<sup>38</sup> was used as exchange-correlation

functional. The energy cut-off for the plane-wave basis expansion was chosen to be 400 eV. A conjugate-gradient algorithm was employed to relax the ions into their instantaneous ground state. Gaussian smearing with a width of 0.05 eV was also utilized. For the surface Brillouin zone integration, a  $2 \times 2 \times 1$  Monkhorst-Pack<sup>39</sup> k-point mesh was used. The convergence criteria for electronic self-consistent iteration and ionic relaxation were set to  $10^{-4}$  and  $10^{-3}$  eV, respectively.

A lithium metal anode slab structure is created using seven layers of lithium metal exposing the lowest surface energy facet (100);<sup>40</sup> the bottom two layers of the slab are fixed to resemble bulk behavior. The total dimensions of the cell including the lithium metal slab are 10.3 Å x 13.8 Å x 33.3 Å. A vacuum layer of ~23 Å added above the Li metal surface in the Z direction, provides the space where the electrolyte is located. A fixed helium layer is added at 3 Å from the top of the cell, to prevent the interaction of the electrolyte with the bottom layers of lithium metal due to the periodic boundary conditions. Lithium ion deposition is studied under different solvents 1,3-Dioxolane (DOL) and 1,2-Dimethoxyethane (DME), commonly used in Lithium-metal based batteries. For comparison, we also use ethylene carbonate (EC), and a 1:1 v/v binary mixture of solvents (EC and DME), mostly used in Li-ion batteries. Schematics of the initial configuration of the system can be found in Figure S1 (Supporting Information).

The electro-neutrality of the cell is maintained through the study. The Li cation of interest is part of ionic pair or a salt ( $Li^+ PF_6^-$  or  $LiFSI$ ). These salts are commonly used as part of the electrolyte in lithium-based batteries. The density of the solution is calculated by first placing the desired concentration of the salt and then packing the free volume with

the density of each solvent DME ( $\rho = 0.87 \frac{g}{cm^3}$ ), DOL ( $\rho = 1.06 \frac{g}{cm^3}$ ) and EC ( $\rho = 1.32 \frac{g}{cm^3}$ ). Further relaxation of solvent molecules is achieved by minimization done via classical molecular mechanics. The minimization with classical mechanics is done using a consistent valence force field (CVFF)<sup>41</sup> as implemented in the Materials Studio software. Structures were optimized and subsequent AIMD simulations were performed for 2 ps to further relaxing the system. AIMD simulations were carried out in the canonical NVT ensemble at 330K with a time step of 1 femtosecond. The Nose thermostat<sup>42,43</sup> was used to keep the temperature constant with a damping parameter set to 0.5.

Bader charge analysis was performed<sup>44,45</sup> to study the charge transfer in the system. This method calculates the Bader volume of an atom enclosed by zero flux surfaces and assigns its total electronic charge. Charge density difference of the system including the ion pair and solvent molecules and Li metal slab was calculated using the Equation 1, where  $\rho_{total}$  is the charge density of the system,  $\rho_{salt}$  is the charge density for the ionic pair and  $\rho_{others}$  is the density of all other components including lithium metal slab, solvent molecules and the helium layer. This charge density difference allowed understanding of the charge accumulation or depletion and therefore the effect of the environment that surrounds each atom or molecule at a given location, on the electron distribution.

$$\rho_{difference} = \rho_{total} - \rho_{salt} - \rho_{others} \quad (1)$$

The thermodynamic integration slow-growth approach was applied to follow the diffusion and evaluate the free energy pathway of the cation step by step starting from an initial location in the electrolyte phase, until it is desolvated and deposited on the lithium metal surface. The thermodynamic integration simulations were carried out using the Blue Moon

ensemble method as implemented in VASP. This technique allows us to study the activation barriers involved in the cation deposition and therefore identify relevant steps during the trajectory.<sup>31</sup> The collective variable ( $\xi$ ) is defined as the reaction coordinate that defines the motion of the lithium cation from an initial location  $\xi_1$  towards a defined location  $\xi_2$  in the lithium metal slab with a small step size of 0.0008 Å every femtosecond. Every step in this trajectory provides a free energy gradient ( $\delta F/\delta \xi$ ), the value of the free energy gradient is obtained by averaging the dynamic trajectories over 100 fs, and the free energy  $\Delta F$  is calculated as a path integral along an arbitrary path between  $\xi_1$  and  $\xi_2$ .<sup>31</sup>

$$\Delta F_{1-2} = \int_{\xi_1}^{\xi_2} \left( \frac{\delta F}{\delta \xi} \right) d\xi \quad (2)$$

This AIMD-based thermodynamic integration approach has been used in many different fields<sup>46-49</sup> and additional information about the method can be found in other references.<sup>32,50,51</sup>

## Results and Discussion

### *Cation Deposition Mechanisms: Solvent Effects*

We first studied the effect of the solvent chemistry and structure on the deposition of  $\text{Li}^+$  on lithium metal surfaces using DFT optimizations and evaluation of charge transfer. In this part of the work, the initial positions for the lithium cation and  $\text{PF}_6^-$  anion were kept the same for all systems. Solvent molecules were added into the free volume of the simulation cell on top of the Li metal slab, and minimized by using classical mechanics. Figure 1 and Figure 2 show the final DFT optimized structure of the systems that contain

DME and EC respectively. The initial structures of each system are displayed in Figure S2. Detailed information about number of solvent molecules, lithium atoms and other components are reported in Table S1 of Supporting Information.

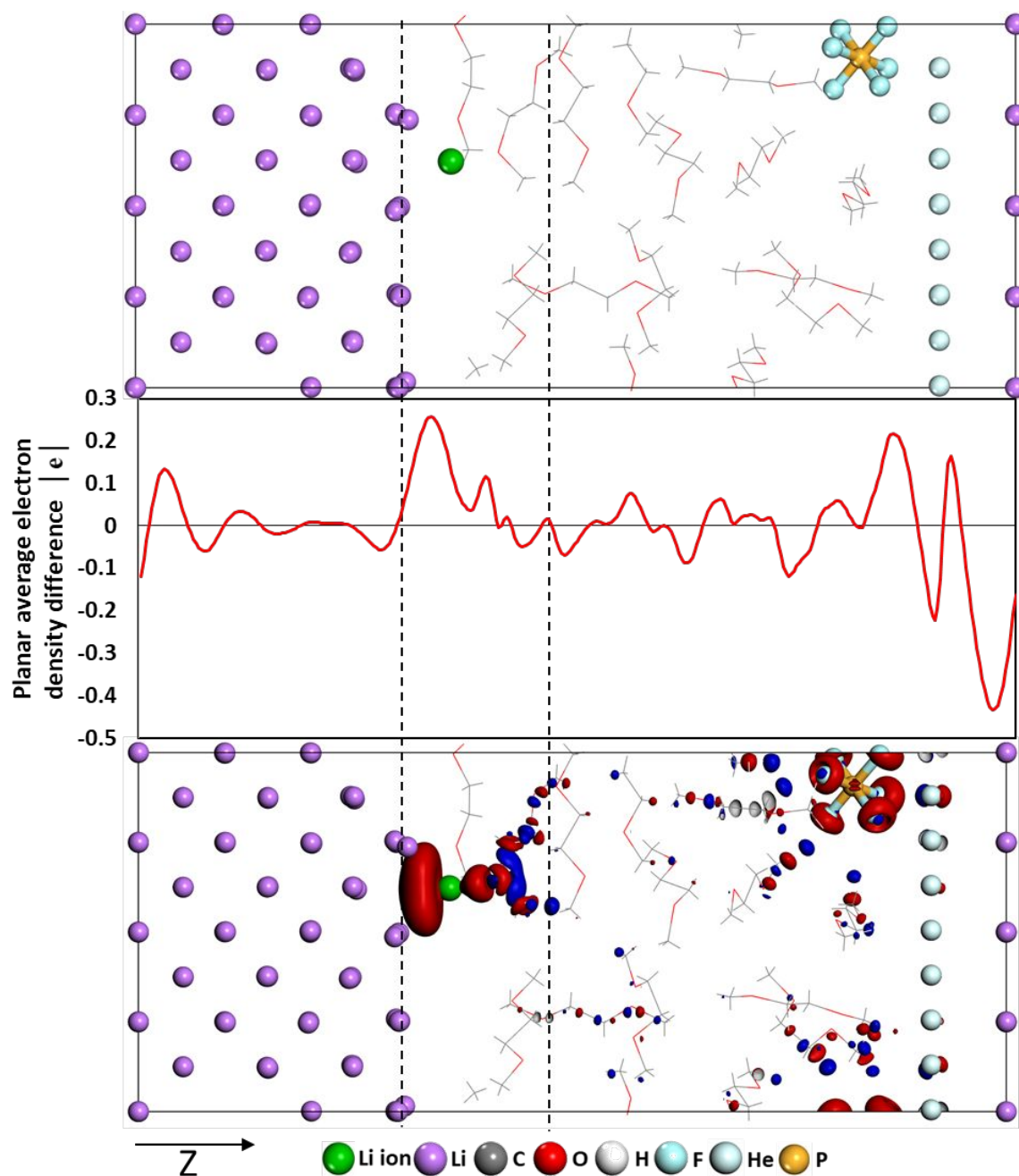


**Figure 1.** Snapshot of cation deposition structure with DME as solvent (top), planar average electron density difference  $\Delta\sigma(z)$  curves (middle), and charge density difference diagrams (bottom) (isosurface level =  $5.0e-4$ ). In the charge density difference distribution diagrams, red represents the electron accumulation area, while blue is the electron depletion area. Grey areas are the cross-sections of the charge density difference.

The planar average electron density difference  $\Delta\sigma(z)$  (middle plot) in Figure 1 was evaluated in small volume elements perpendicular to the Z axis and the excess (or deficit) electrons at each z position are indicated by the positive and negative regions. Optimized structure in Figure 1 (Top plot) shows  $\text{Li}^+$  (green atom) close to the lithium metal slab and surrounded by DME solvent molecules, the interface of interest is the one shown within the dash black lines. Figure 1 (bottom) shows red regions surrounding the lithium-ion and corresponding to the peaks in the middle plot, indicating electron accumulation area, calculated according to equation (1). If additional lithium cations would become close to this region (red - electron accumulation), they would migrate and deposit close to that area creating non-uniform deposition. This was shown in previous research that studied the deposition of  $\text{Li}^+$  ions on Li metal surface with defects such as a single deposited Li atom.<sup>52</sup> Various adsorption sites were tested for the preferred deposition site of a Li cation. It was found that this preferred location is a hollow site available next to the defect in the metal surface. Moreover, this deposition mode in interstitial sites was confirmed by *ab initio* analysis of growth of Li metal nanoclusters that determined the preferred locations of addition of a Li cation by evaluation of the electrostatic potential in Li metal clusters of increasing size.<sup>27</sup>

The electron depletion areas (blue, Figure 1) can be found on the DME molecules and they are correlated to the negative values in the middle plot. The net charge of the lithium-ion changed from approximately  $+1|e|$  to  $-0.87|e|$  after optimization based on Bader charges. Although, Bader charge analysis does not yield reliable results when used on lithium metal atoms<sup>53</sup> due to the creation of 'pseudoatoms' that contain electron accumulation in regions where there is no nuclei, the charges are well described for Li ions. In addition, in this study the Bader charge is used along with an alternative method. The electronic density difference profile shown in the middle plot represents the plane-averaged electron density difference  $\Delta\sigma(z)$  calculated from the DFT calculated electron densities evaluated in planes perpendicular to the z-axis, within thin slabs (of width  $\delta z$ ) along the z direction. This function  $\Delta\sigma(z)$  shows directly the average accumulation or deficit of electrons as a function of z, that is created due to the interactions of the electrolyte phase with the Li metal surface. As such,  $\Delta\sigma(z)$  provides a better understanding of the possible redox reactions at the interface and the cation deposition phenomena.

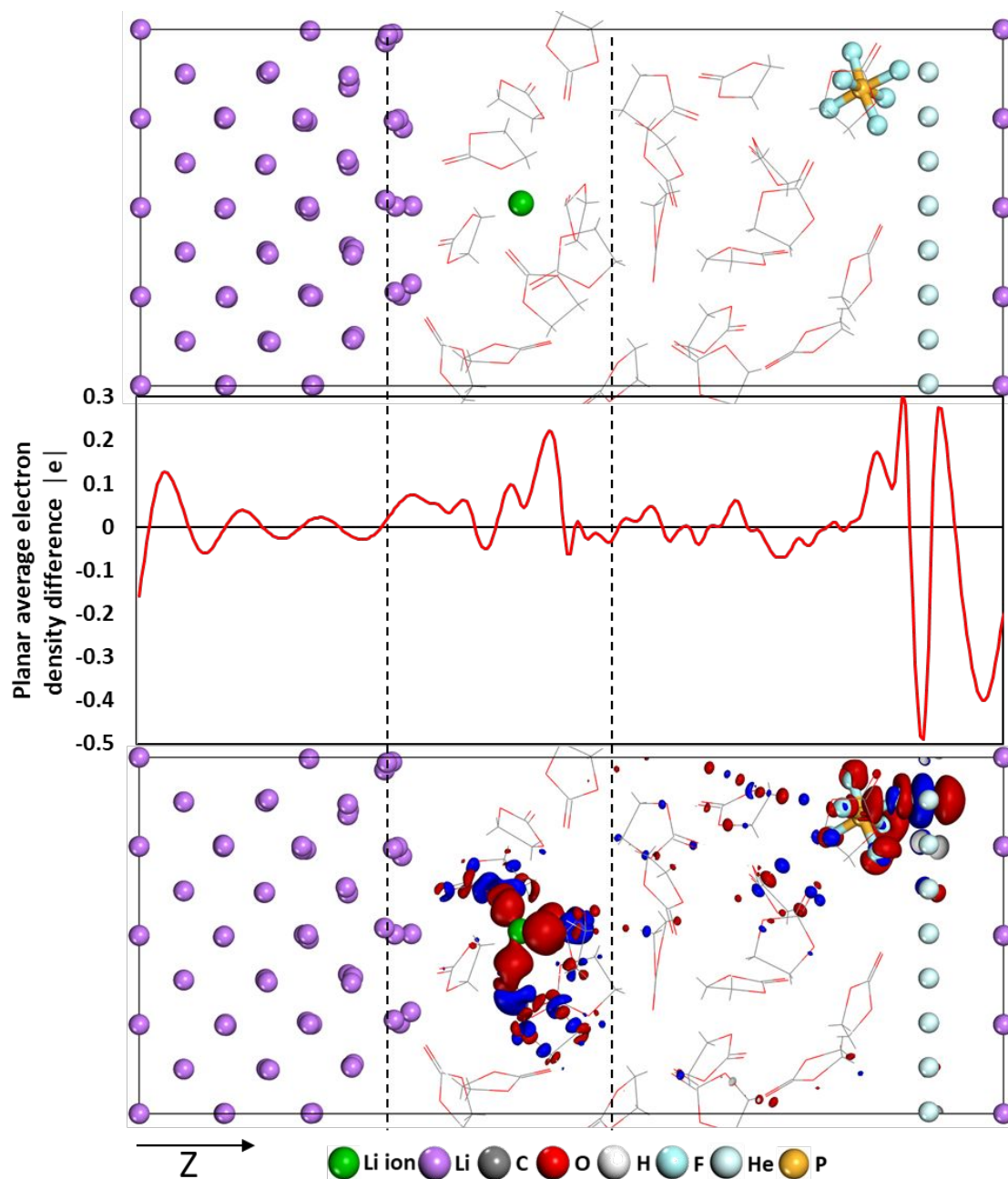


**Figure 2.** Snapshot of cation deposition structure with EC as solvent (Top), planar average electron density difference  $\Delta\sigma(z)$  curves (middle) and charge density difference diagrams (bottom) (isosurface level =  $5.0e-4$ ). Color code as in Figure 1.

Figure 2 shows the optimized system when EC is used as a solvent, lithium-ion (green atom) remains solvated in the electrolyte phase and far from the lithium metal slab compared with the lithium ion on Figure 1. The net charge of the lithium-ion is  $+0.87|e|$  and it is surrounded by electron accumulation areas. The electron accumulation areas (red) in Figure 2 are located on the solvent molecules. As shown below, the top EC molecule has received around  $-0.86|e|$  located near the carbonyl carbon. This reduction of the EC molecule causes the molecule no longer being planar. The electron localization and geometrical change are in agreement with previous DFT calculations of the EC reduction.<sup>54</sup> The  $PF_6^-$  anion located at the right of the cell is not fixed and it interacts with the He layer that is also fixed. The peaks (and opposite valleys) found at the right side in the middle plot on Figure 2 correspond to the Helium layer being fixed, and its charge being almost neutral. The detailed electron density difference distribution is quantified in the middle plot, that shows that the electron accumulation in this case occurs near the reduced solvent. Note that there is still some electron accumulation at the interface but much lower than in Figure 1. Table 1 shows that even though the lithium metal slab loses the same amount of electrons for both systems in Figures 2 and 1 (EC and DME), in Figure 2 EC is reduced instead of the lithium-ion. The Li-ion remains with its initial charge because of the much higher electron affinity of EC compared to DME.<sup>55</sup> Peaks on the electron density difference profile in Figure 2 indicate the excess of electrons, in the planes that include the solvent molecules involved in the solvation shell.

The Density of States (DOS) shown in Figure 3 is helpful to characterize the electronic structure of the lithium ions present in both systems. In contrast to the lithium-ion that is not reduced (red line in Figure 3), the reduced lithium-ion in the DME case (blue line in

Figure 3) shows a high population of electronic states around the Fermi energy revealing the reduced state. The charge transfer that occurs from the lithium metal to the lithium-ion in DME, changes the electronic structure as well as induces the desolvation, which causes the Li atom to become closer to the surface 1.7 Å, compared to the final ion distance in the system with EC of 4.3 Å (the initial placement of the lithium cation in both cases is 4.6 Å from the surface).

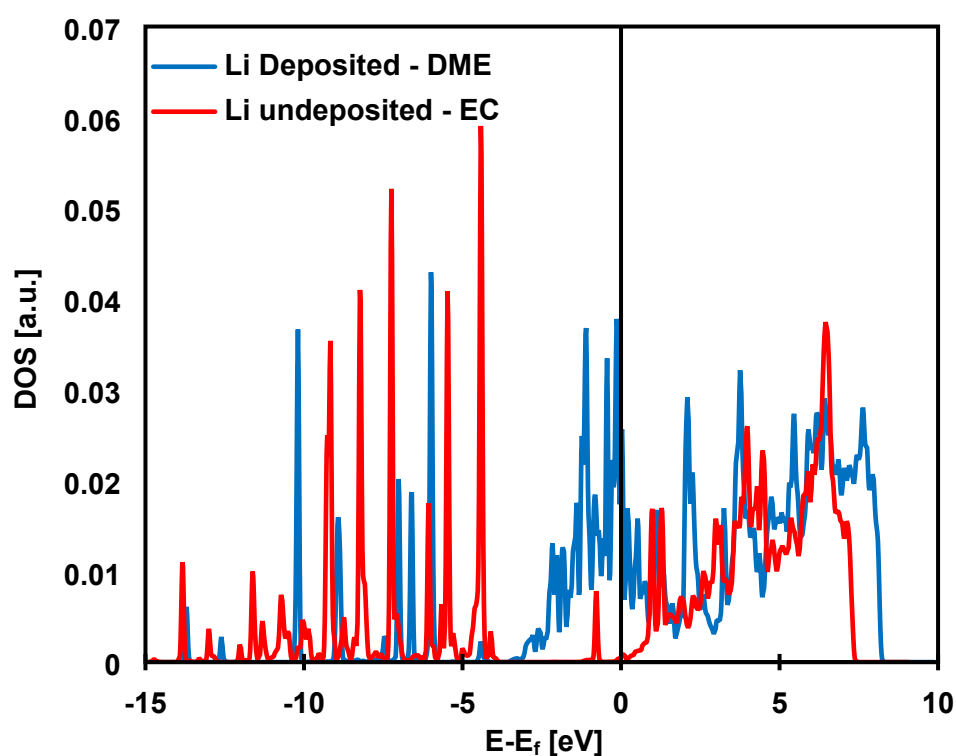
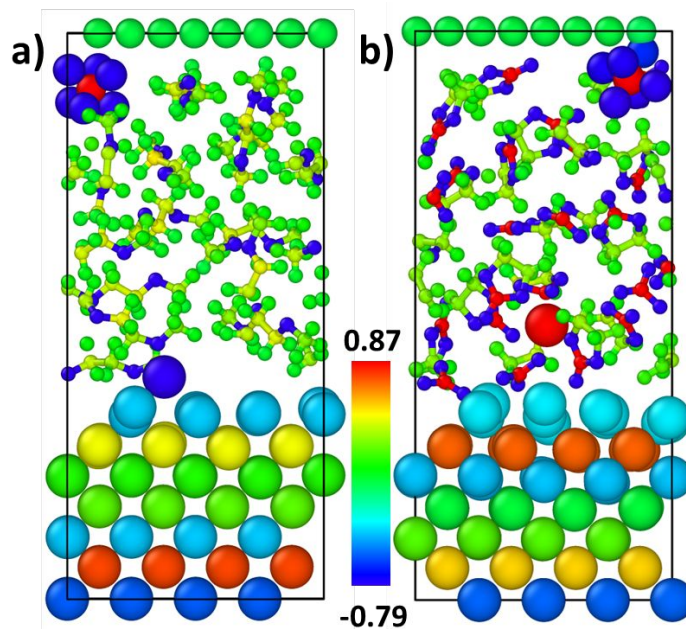


**Figure 3.** Density of States of Li atom for the cation examined in Figures 1 and 2. Reduced deposited lithium-ion in the DME solvent is represented by the blue line. Solvated lithium-ion in the EC solvent is shown in red.

**Table 1.** Bader net charge ( $e$ ) after DFT optimization including each component in the simulation cell. The charges for a given species are total (include all atoms and/or all molecules).

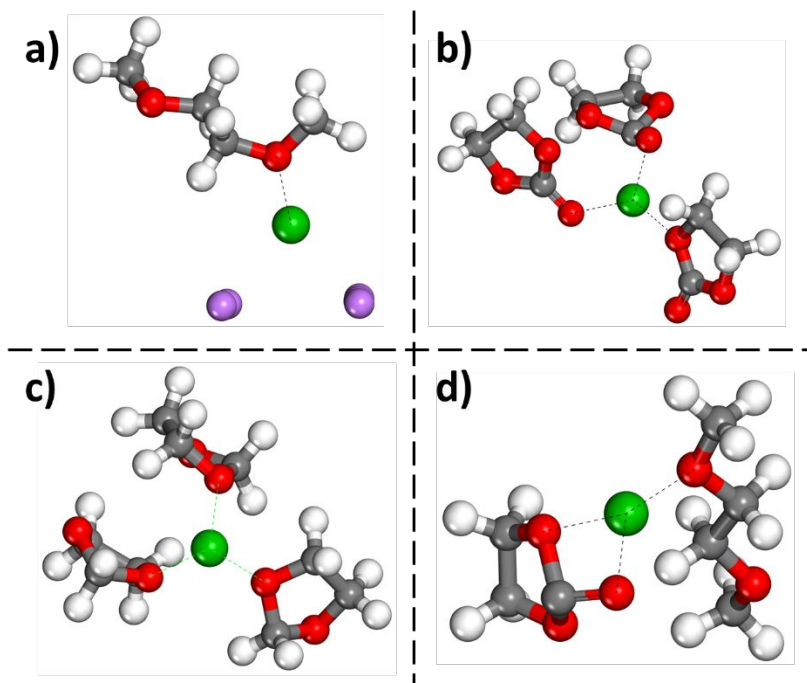
	<b>DME</b>	<b>EC</b>	<b>DOL</b>	<b>EC-DME</b>
<b>Li Metal Slab</b>	2.53	2.43	1.09	2.66
<b>Solvent</b>	-0.44	-2.04	-0.67	-2.29
<b>Li Ion</b>	<b>-0.80</b>	<b>0.86</b>	<b>0.87</b>	<b>0.87</b>
<b>PF<sub>6</sub><sup>-</sup></b>	-0.98	-0.88	-0.90	-0.87
<b>He</b>	-0.32	-0.37	-0.39	-0.37

Table 1 shows the overall net charge of each component (including all molecules or atoms of a given component) after optimization. The net charge of the anion as well as the helium layer are similar for all systems. The drift of negative charge to the He atoms is an artifact of the simulation setting but it does not affect the discussion that is focused on changes in the electronic density near the cation. The main differences in charges are in the lithium metal slab, solvent, and lithium cation. Although the lithium metal slab loses a similar number of electrons for systems based on DME or EC (Table 1), the distribution of the charge within the layers of the slab is different in each case. Figure 5 shows the average net charge per layer on the lithium metal slab.



**Figure 4.** Average per layer Bader charge distribution in lithium metal slab a) DME used as a solvent b) EC used as a solvent.

Figure 4a shows the charge distribution within the slabs as the cation approaches the lithium metal slab surface. The bottom two layers of the lithium metal slab are fixed and the total net charge of those layers added up is zero. In Figure 4a layers 3, 4, 5, and 6 (counting from the bottom up) change from negative (light blue) to neutral and then positive (layer 6 yellow), the top layer (7) is negative. Here, we could see the dynamics of electron transfer from the bottom to the top layers of the lithium metal slab that makes them available to reduce the cation, or in other systems starting the SEI formation by initiating the reduction of the solvent. The main difference within Figure 4a and 4b is that in the 2<sup>nd</sup> case the top three layers alternate negative, positive and negative due to the electron transfer to the EC molecules.



**Figure 5.** Solvation shells formed around lithium cation for different solvents in the electrolyte a) DME, b) EC, c) DOL and d) EC-DME. (Color code as Figure 1) The first two structures correspond to the DFT optimized structures shown in Figures 1 and 2.

The electrolytes in Li metal batteries drive Li ions motion during the charging and discharging process. Cyclic carbonate solvents increase the salt solubility but the mobility of the ions slightly decreases. On the other hand, linear carbonates increase the mobility of ions but the salt solubility decreases.<sup>56</sup> The solvation shells around the lithium cation shown in Figure 5 are the configurations (close up of the optimized structures in this work) in which the solvent molecules are organized around the lithium cation. Other more complex structures may arise as previously reported.<sup>57</sup> Lithium mobility and ability of the cation to be deposited on the lithium metal slab is affected for the structure of these solvation shells, which also change as they become close and are affected by the electrified interface.

The structure of the lithium solvation sheath in lithium-based batteries is important in the SEI formation because the solvents in the solvation sheath predominantly participate in forming the SEI by preferential reduction at potentials higher than that of Li ion reduction and even by spontaneous reaction of the electrolytes in contact with Li metal at open circuit conditions.<sup>56,58,59 60</sup> Comparing Figures 5 a and b we could examine further why the cation is reduced and deposited on the surface in the first case but remains solvated by the EC molecule and not reduced in the second case. Reduced ion mobility and the strong solvation shell (high Li<sup>+</sup> coordination number with O) that is created with the highly polar and easily reducible cyclic solvent (EC) are the reasons for this behavior.

The solvation shell created by the DOL molecule (Figure 5c) is structurally similar as the one created by EC; however due to the much lower electron affinity of DOL, neither the solvent nor the cation are reduced (Table 1). Additionally, the electron density analysis can be found in Figure S3, where the similarity with EC solvation shell can be observed, as areas of electron depletion and accumulation are observed. When there is a mixture of solvents (EC/DME, Figure 5d), the trend of the ion to relocate is increased but the solvation shell shown in Figure 5d still prevents the cation deposition and reduction. Figure S4 shows the asymmetry on the charge depletion and accumulation areas. Although the cation gets closer to the surface the electron affinity of the EC molecules promotes their reduction instead of that of the cation.

#### *Effect of anion-cation distance and salt concentration*

During the actual contact between the electrolyte solution and the electrode surface, numerous configurations of the cation may arise. Moreover, if there is an applied field, the surface could have a much different charge profile than that discussed here. In this

study, we considered alternative initial configurations for most of the systems. An important case highlighted next is the effect of the distance between the anion and the cation. Figure 6 shows two additional initial configurations, where the electrolyte molecules and cation are kept in the same initial positions as in Figure 1. Configuration 2 (Figure 6a) has the anion located at the middle part of the electrolyte region. Configuration 3 has the anion separated from the cation but close to the surface, although after optimization (Figure 6c) both anion and cation end up near the surface but separated from each other. The distances from the cation to the center of the anion after optimization were 6.8 Å and 5.2 Å in Configurations 2 and 3 respectively. It is important to notice that the initial distance of the cation to the metal surface is the same (4.6 Å) as in Figure 1. These two structures highlight different aspects. Figure 6b shows the interaction between solvent, anion, and cation where the cation keeps its charge of  $\sim 0.87$  e. The attraction forces between these salt components inhibits the cation reduction, and the anion is too far from the surface to receive the electron transfer.

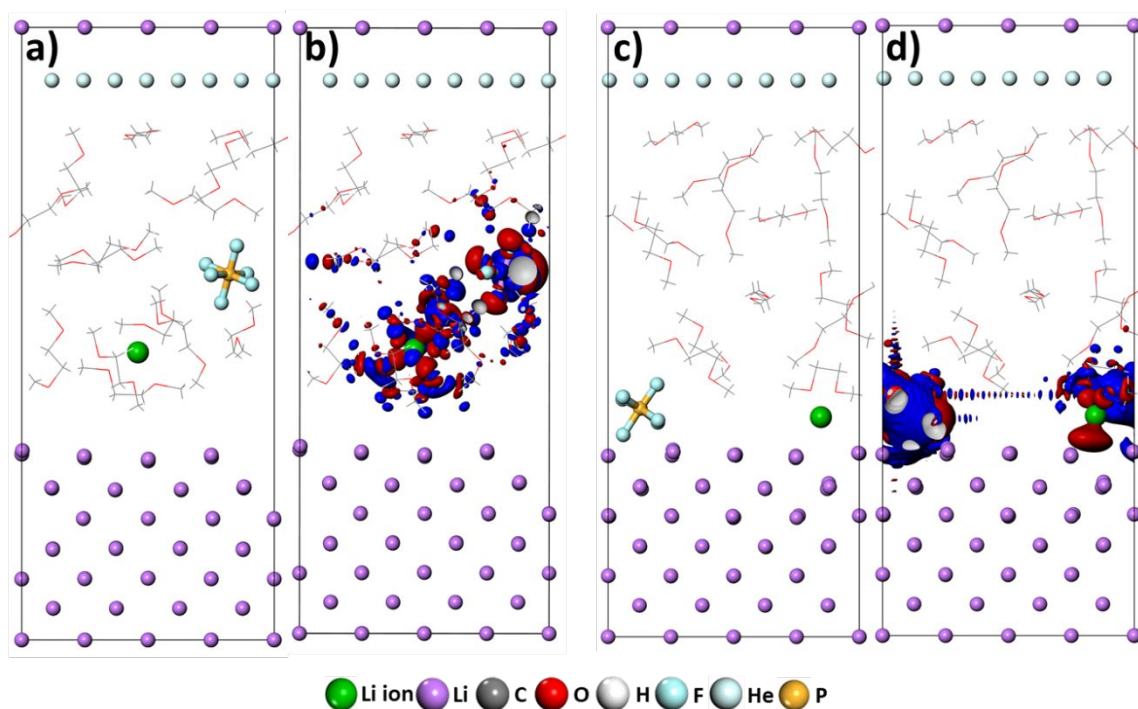


**Figure 6.** Effect of the anion-cation distance on cation reduction and deposition. a) Optimized structure of system at an anion-cation distance of 6.8 Å (Configuration 2). b) Charge density difference diagrams for Configuration 2. c) Optimized structure of system in Configuration 3. d) Charge density difference diagrams for Configuration 3. (isosurface level =  $5.0e-4$ ) Color code as in Figure 1.

Figure 6d shows a final position for the anion even closer to the surface, whereas the anion-cation distance is 5.2 Å (Configuration 3). In this structure, the lithium cation is partially reduced by the electrons transferred from the lithium metal slab with a partial charge of  $\sim -0.54 e$ . It is also important to point out that after a dynamic evolution of the optimized system, the fast anion decomposition is expected due to the complete reduction of the anion by the lithium metal slab. In reality, many different configurations can be encountered, showing that cation deposition is not only a matter of the distance cation

and anion and solvation shell, but is in fact a combination of these factors including the effect of the intrinsic electric field and eventually that of an applied external field.

Similar to the effect of the initial configuration of the systems, the salt concentration affects ion mobility. In this work, several salt concentrations were studied for all solvents previously mentioned. The optimized structures and dynamic snapshots of the systems are depicted along with the most relevant interatomic or intermolecular distances in Figure S5. Figure 7 shows the net charge of all components in the simulation cell for different salt concentrations (0.64 M, 1.3 M and 2 M) for a variety of solvents. Figure 7a shows that the net lithium metal charge decreases as the salt concentration increases, implying less oxidation of the Li metal surface atoms and less electron transfer. This reflects also the negligible DME reduction in all cases, whereas the cation is reduced only for the lowest salt concentration. This could be attributed to the strong interaction of the anion-cation pair as the salt concentration increases. In the cases of EC and DOL (Figures 7b and 7c), the dependence of Li surface oxidation with salt concentration varies slightly: the maximum oxidation is observed at 1.3 M in presence of these two solvents, which demonstrates the solvent power able to mitigate the anion-cation interaction that combines with the higher electron affinity of the solvent. However, at 2M, we see less reduction of EC and DOL than at 1.3 M, suggesting that salt concentration may be a stronger factor than solvent electron affinity for the combined reactivity including Li surface oxidation, and solvent vs. cation reduction. Concentrated electrolytes exhibit higher stability and Coulombic efficiency. This improvement may be explained by the change in solvent-ion coordination structures. Several studies have focused on these phenomena. In dilute electrolytes the most common structure found is solvent-separated

ion pairs. Such structure shifts to contact ion pairs, and cation-anion aggregate structures when the salt concentration increases. As a result, the number of uncoordinated solvent molecules decreases leaving fewer molecules prone to reduction by the Li metal, leading to a more stable solvent.<sup>16,61</sup> Moreover, as discussed in recent work,<sup>61</sup> the ability of the anions to coordinate with multiple lithium-ions lowers the anion LUMO levels below those of the solvent molecules. Thus, as salt concentration increases, the anion becomes reduced instead of the solvent.

Figure S6 in supplemental information has been added illustrating coordination structures found at two different concentrations in this study. A direct consequence of the change in coordination structures includes an SEI layer derived mainly of anion decomposition rather than solvent decomposition, which in several cases could enhance the SEI qualities.<sup>16,61-63</sup>

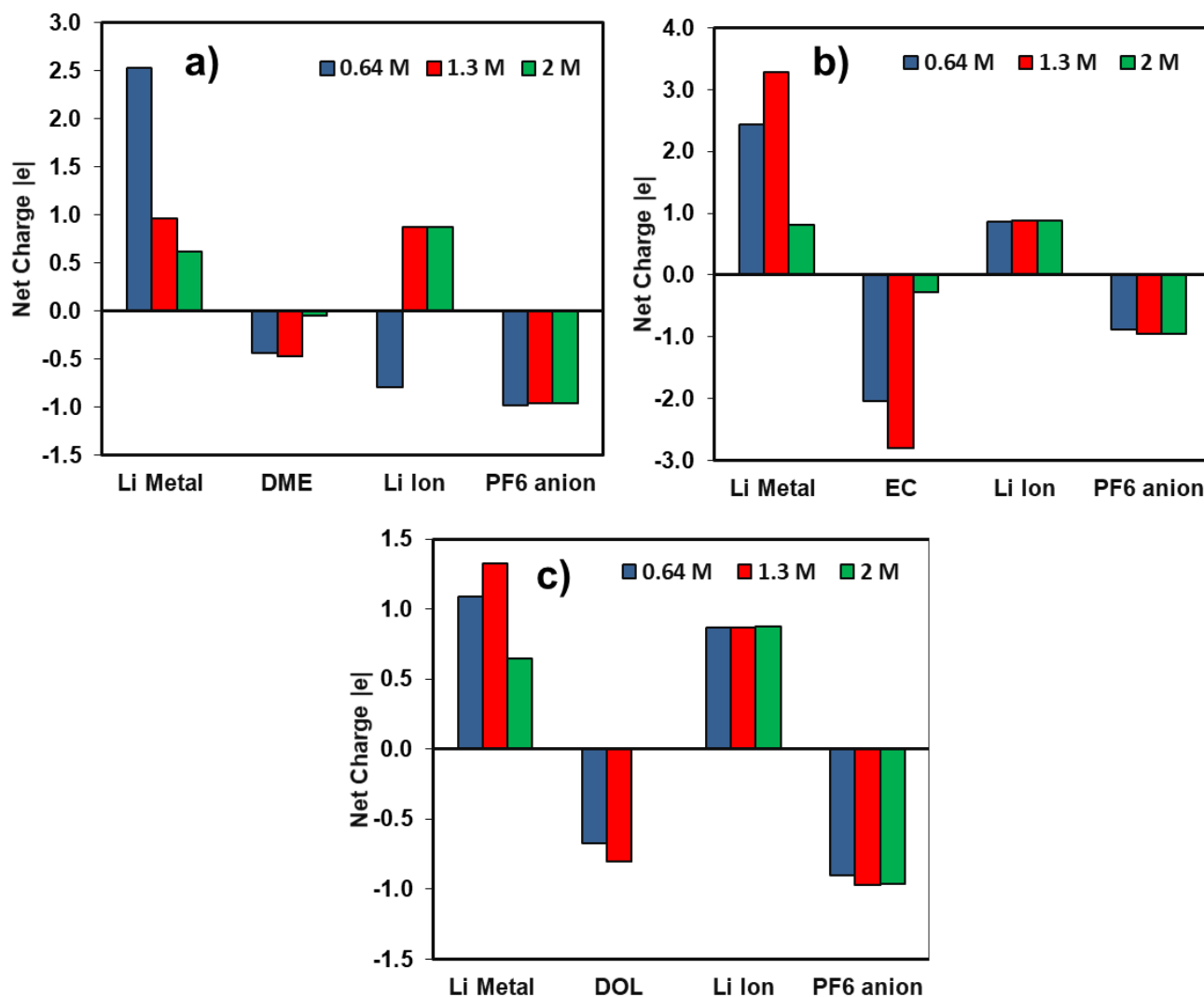


**Figure 7.** Net charge for the Li metal slab and electrolyte components at three salt concentrations for solvents: a) DME b) EC c) DOL. The net charge is calculated by adding all the charges of the molecules in a given species, except for those of the anion and cation, that are calculated per molecule.

### *Ionic motion from the electrolyte to the surface: Slow growth approach*

The solvation shell formed around the lithium-ion can be complex and strongly limiting for the mobility of the cation; this is an important issue for elucidating the lithium deposition mechanisms using AIMD simulations. The thermodynamic integration slow growth

approach to determine the free energy profile of a given dynamic trajectory is a very useful tool that allows us to follow the motion of an atom in a certain direction without imposing any specific path.

Figure 8 shows the slow growth analysis in a system displaying the trajectory of one lithium cation (red atom) initially solvated by one DME molecule ( $\xi_1$ ) that has one atom on the lithium metal slab as its final destination ( $\xi_2$ ). This instruction (defining initial and final positions) is also called collective variable ( $\xi$ ). The motion proceeds with a small step of 0.0008 Å. While the ion reaches a new position given by this step, a free energy gradient calculation ( $\delta F/\Delta\xi$ ) is done by averaging the dynamic trajectories over 100 fs. Figure 8a is the initial structure at which the lithium cation is initially solvated by one DME molecule. The initial structure is constructed as previously described for the DFT calculations (Figure 1), where after the initial placement of the cation and anion pair (1M LiPF<sub>6</sub>) the cell is packed with solvent molecules until the desired density is obtained. Next, the system is optimized with classical mechanics as described in the computational methods. Finally, the constrained AIMD is carried out. Figure 8b depicts the change in free energy  $\frac{\delta F}{\Delta\xi}$  [eV/Å] as well as the integrated free energy profile  $F$  [eV] of the system during the cation deposition calculated with equation (2).

The collective variable ( $\xi$ ) is defined in this case as the lithium cation getting away from the oxygen atom in the initial solvation shell and approaching a lithium metal atom in the slab. The total free energy profile shows that the free energy initially decreases (favorable process) representing the movement from the initial solvation shell (shown in 1\*) in which the cation is solvated by one oxygen atom (yellow lines in the figure indicate closer oxygen

atoms) and it moves to a second solvation shell (Figure 8 snapshot 2\*) in which the cation becomes more favorably solvated by three oxygen atoms. The energy starts to increase and there are several barriers detected during the trajectory. The following event (2\* → 3\*) is the diffusion out of the stronger solvation shell created by the three DME solvent molecules; this energy barrier is ~0.24 eV (This barrier is calculated as the difference between the energy values of snapshot 3\* and 2\*) and leads to the cation no longer being solvated by several oxygen atoms and facilitating its motion in the direction of the surface and therefore its deposition. Additional barriers shown after 3\* illustrate events that are less likely to happen at least in absence of a driving force such as an external potential. In this system, the lithium cation that has already been reduced will not penetrate the lithium metal slab as suggested by the magnitude of the barrier.

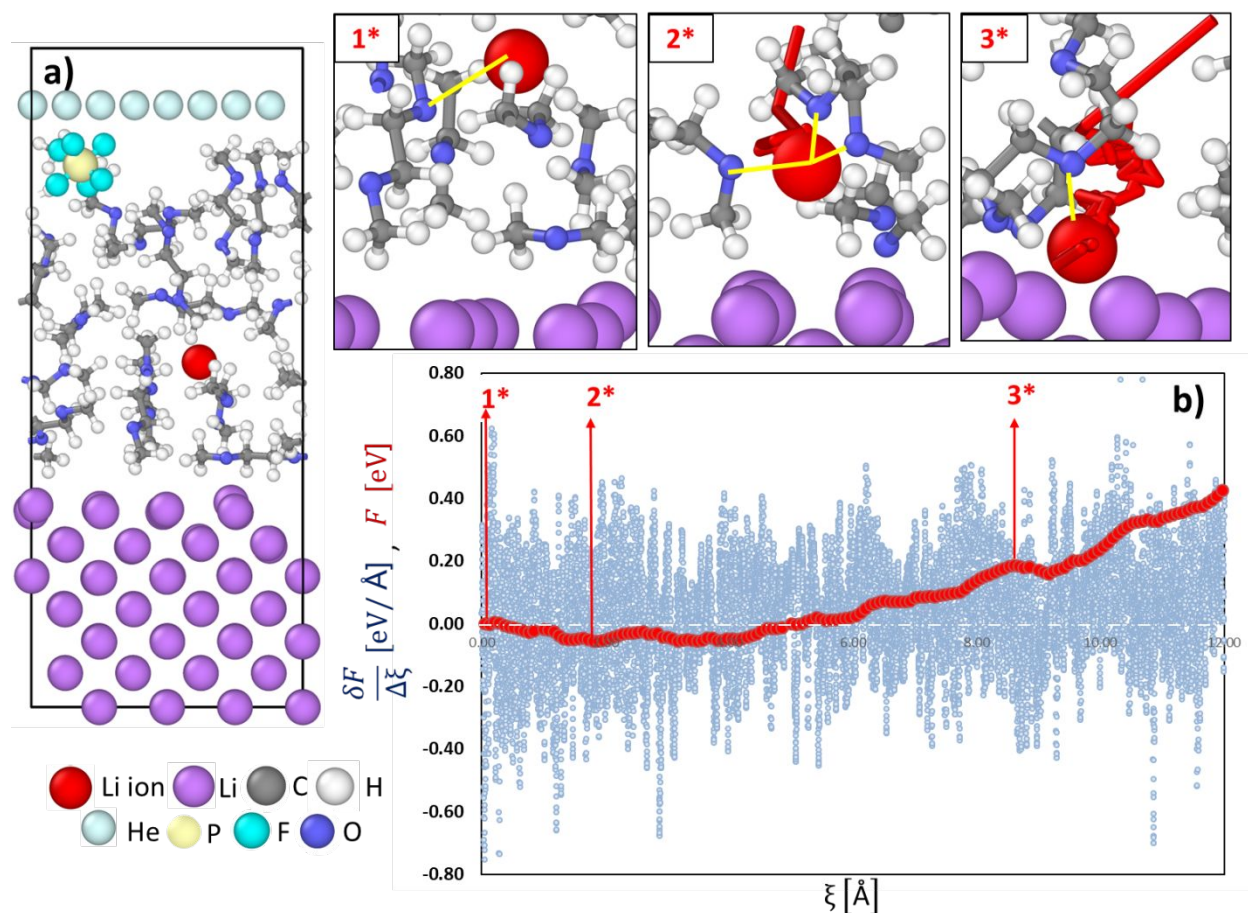


**Figure 8.** Free-energy profile of lithium cation deposition from an electrolyte where DME is used as a solvent. a) Initial structure. b) Free energy profile ( $1^* \rightarrow 3^*$ ) snapshots of the lithium cation diffusion pathway and deposition (yellow lines indicate oxygen atoms in solvation shell).

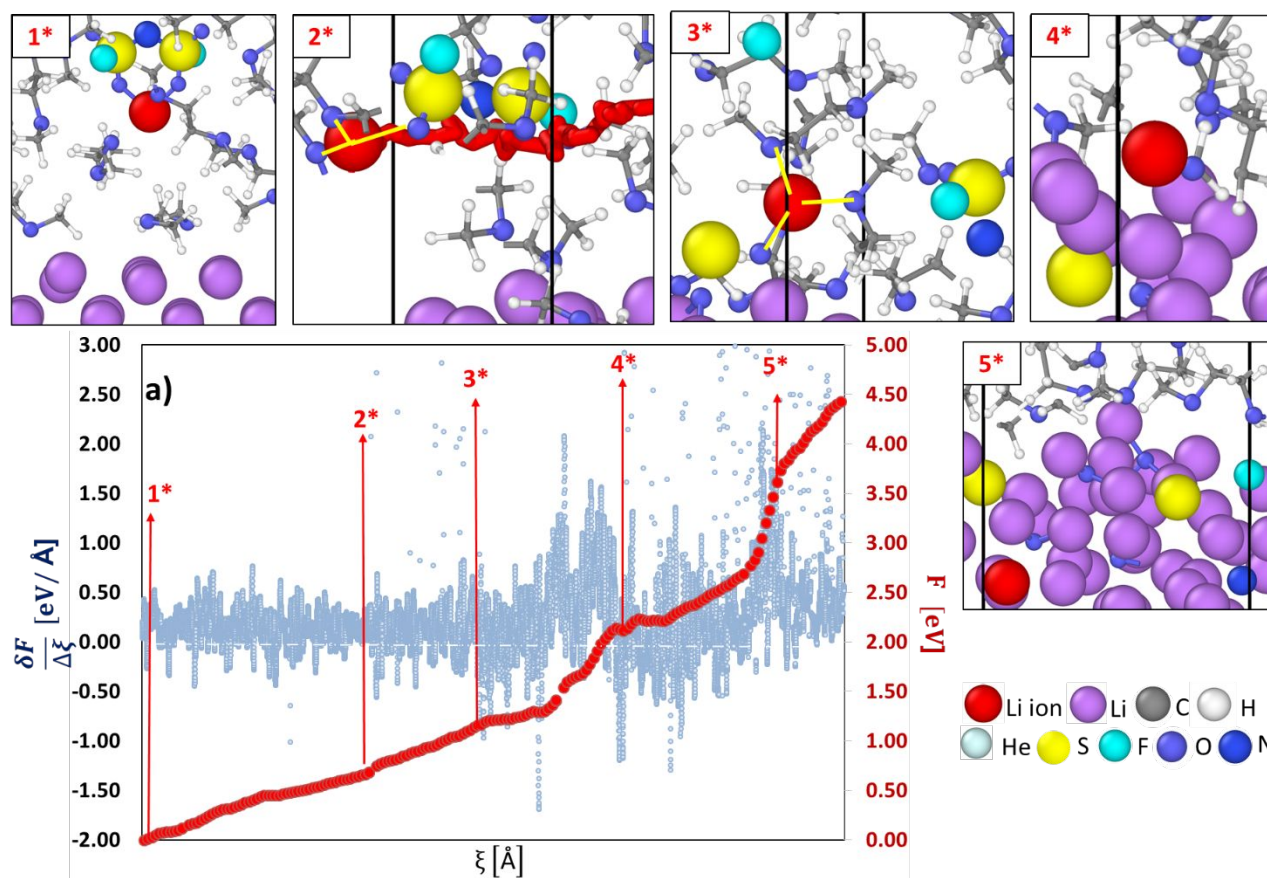
Figure 9 illustrates similar pathway for an initial ion-pair structure. In Figure 9 snapshot  $1^*$  the initial structure and solvation shell of the cation includes the counterpart anion, this implies a harder-to-leave solvation shell and therefore the diffusion energetics may vary. Here the *collective variable instruction* is for the cation to get apart from the anion and move towards the lithium metal slab. Although the instruction is similar to that in the previous system, the strong electrostatic interaction within the ionic pair leads to the cation dragging the anion towards the lithium metal surface. In this step ( $1^* \rightarrow 2^*$ ) three

oxygen atoms from solvent molecules try to pull the cation apart from the anion resulting in an energy barrier of  $\sim 0.7$  eV. Energy barriers are calculated as the difference of the energy values  $F$  [eV] between two steps. The following step ( $2^* \rightarrow 3^*$ ) has an energy barrier of  $\sim 0.53$  eV. This new barrier may account for different events that take place until this point, such as the partial reduction of the anion (one fluorine atom that remains solvated in the electrolyte phase) and the diffusion of the ion pair as a whole. In this diffusion pathway the anion is dragging the cation towards the lithium metal slab. The initial distance of the cation to the top layer of the lithium metal slab is  $\sim 6$  Å and such distance is shortened to  $\sim 3$  Å at mark  $3^*$ .

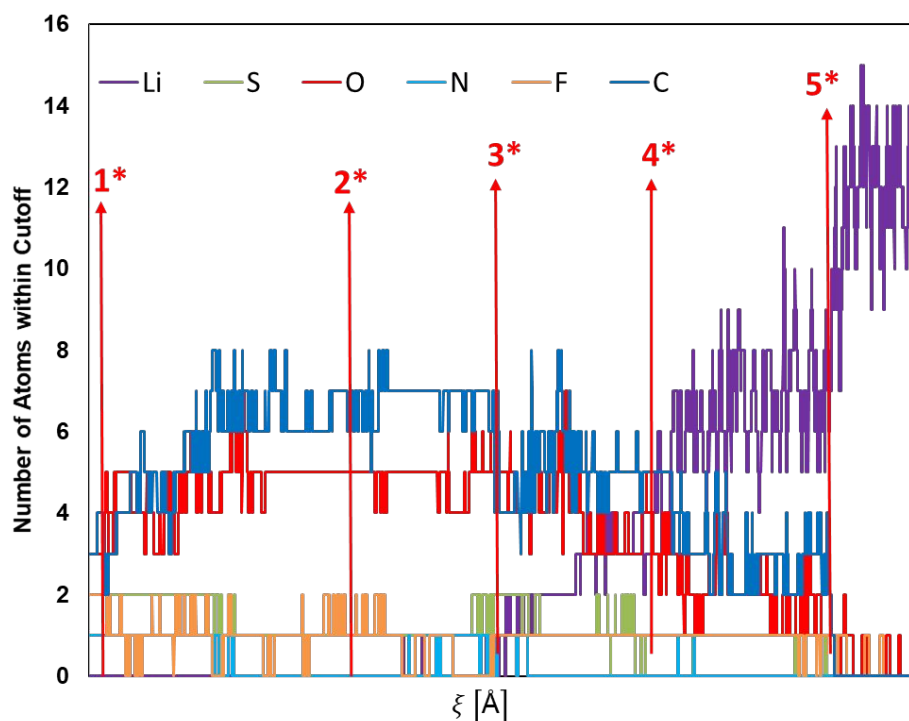
The anion further reduces into atomic species and small fragments forming initial SEI components and the lithium cation deposits ( $3^* \rightarrow 4^*$ ) at the point where it is free of the anion after overcoming an additional barrier of  $\sim 0.98$  eV. The reduction of the decomposition of the anion goes from charged fragments like  $SO_2$  and  $NSO_2$ , all the way to elements forming initial stages of the SEI, like  $Li_2O$  and  $LiF$ . From  $4^*$  forward, the cation diffuses throughout a combination of nucleating SEI/fresh lithium solid slab surface that leads to an increase in the energy barrier to reach its final destination. In addition to the energy barriers calculated by the thermodynamic integration slow-growth method, the structure and elemental composition of the solvation shells around the lithium cation were studied and discussed next.

Figure 10 shows the elements most commonly found in the solvation shell during the lithium cation diffusion and deposition pathway. In this plot labels  $1^*$  through  $5^*$  correspond to the snapshots presented in Figure 9. From the beginning  $1^*$  to  $3^*$  we can see that the majority of atoms present in the solvation shell are carbon (from the solvent)

and oxygen (both from the salt and the solvent molecules). Also, atoms (sulfur, fluorine, and nitrogen) that belong to the anion of the salt are present in this initial stage. At 4\* we see changes corresponding to the actual deposition of the cation. At this point there is a shift from carbon and oxygen being the majority components of the solvation shell to lithium in the metal slab being mostly around of the atom (explanation of how this type of plot was constructed is in the Supporting Information, along with Figure S7).



**Figure 9.** a) Free-energy profile of lithium cation deposition when the anion FSI<sup>-</sup> is part of the solvation shell. Images 1\* through 5\* snapshots of the lithium cation diffusion pathway and deposition. The red line shown in 2\* is the path that the cation has followed until that snapshot.



**Figure 10.** Evolution of the solvation shell atomic distribution as a function of the collective variable.

Different strategies are being studied to prevent dendrite formation as well as for improving the stability of the SEI. Localized high-concentration electrolytes (LHCEs) are used for this purpose. Ideally, a diluent has the appropriate coordination that enables a low viscosity while maintaining the  $\text{Li}^+$  solvation structure observed in high concentrated solutions, although these structures are localized within the electrolyte.<sup>61,64</sup> A diluent suitable for ether-based systems tris(2,2,2-trifluoroethyl)orthoformate (TFEO) has been recently studied due to its advantages for improving the anode as well as the cathode performance in lithium metal batteries.<sup>65</sup>

However, as shown above, the environment that surrounds the  $\text{Li}^+$  affects the diffusion pathway as well as its deposition. Figure 11 shows the slow growth analysis done on a

system that has the TFEO diluent as part of the electrolyte components with the LiFSI salt and DME as a solvent; the initial configuration is shown in Figure 11a. The electrolyte contains DME, TFEO, and LiFSI with a concentration of 1 M. The collective variable ( $\xi$ ) is defined in this case as the lithium cation separating from the oxygen atom in the FSI<sup>-</sup> anion and approaching a lithium metal atom in the slab. The main difference within this system and the one in Figure 9 is that from the initial structure to label 1\* (Figure 11a → 1\*) the Li<sup>+</sup> cation separates from the FSI<sup>-</sup> anion before it diffuses, leading to the cation being able to move without dragging its counterpart. The energy barrier for this step (Figure 11a → 1\*) is high: ~2.95 eV. This is the result of the energy required to overcome the electrostatic attraction in the salt as well as part of the barrier for diffusion of the cation. In the deposition step (1\* → 2\*) the Li<sup>+</sup> cation is solvated by oxygen atoms as well as close to two fluorine atoms in the TFEO molecule leading to an energy barrier for diffusion of ~ 1.41 eV.

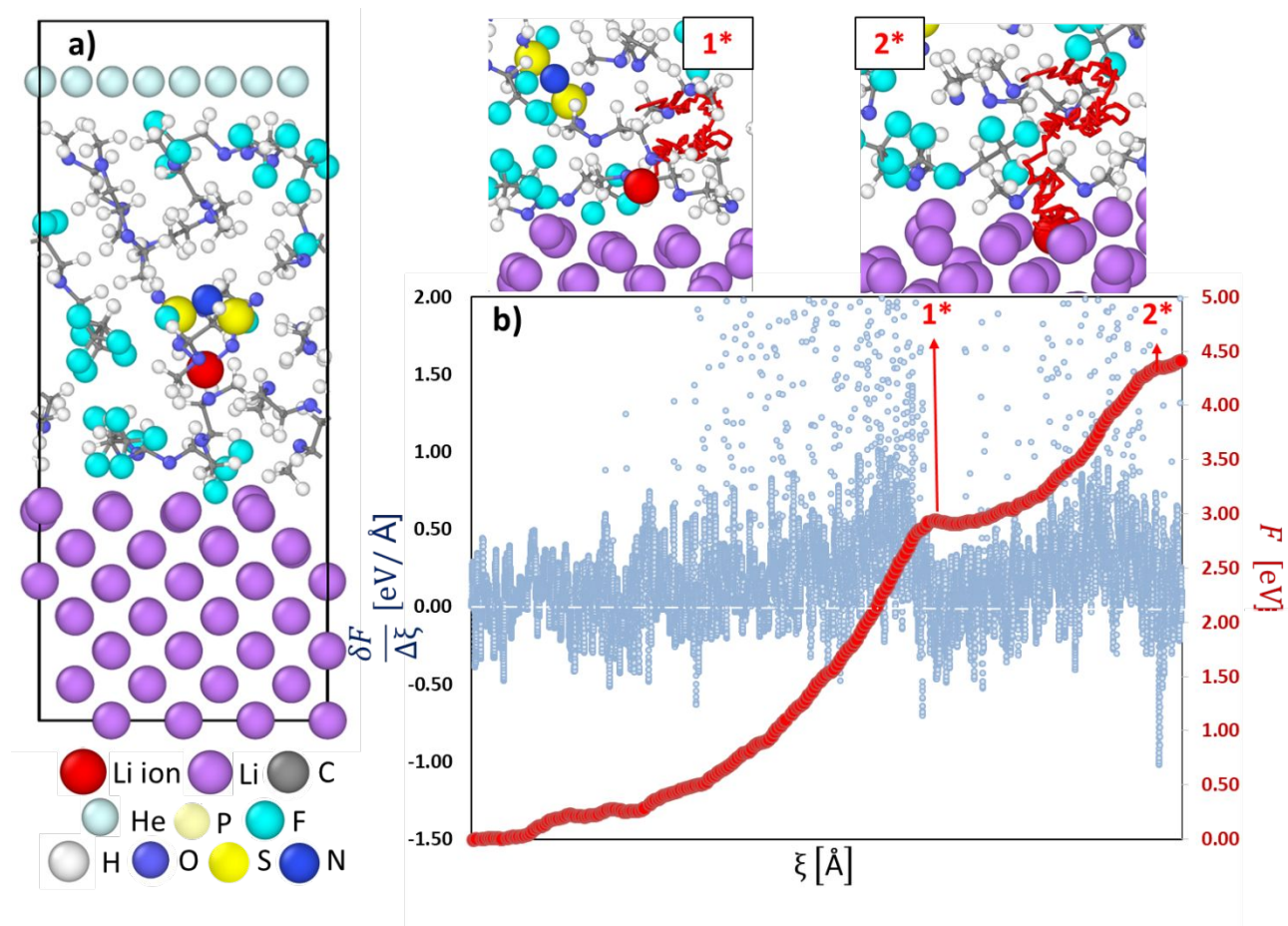


**Figure 11.** Free-energy profile of lithium cation deposition where the anion FSI<sup>-</sup> is part of the solvation shell, and the electrolyte contains DME solvent and TFE0 diluent. a) Initial structure. b) Free energy profile, snapshots (images 1\* and 2\*) of the lithium cation diffusion pathway (illustrated by the red line) and deposition.

In addition to the electrolyte variations like the presence of different salts, solvent, and diluent, the  $\text{Li}^+$  diffusion pathway and deposition is affected by the presence of SEI. Figure 12 shows the slow growth analysis when a nucleating lithium fluoride (LiF) model solid electrolyte interphase is located on top of the lithium metal slab. The LiF layer shown in Figure 12a was generated in AIMD simulations by the reduction of two  $\text{PF}_6^-$  anions.

During battery cycling, the LiF layer can be attributed also to the decomposition of other salt anions as well as higher fluorinated diluents like TFEO.

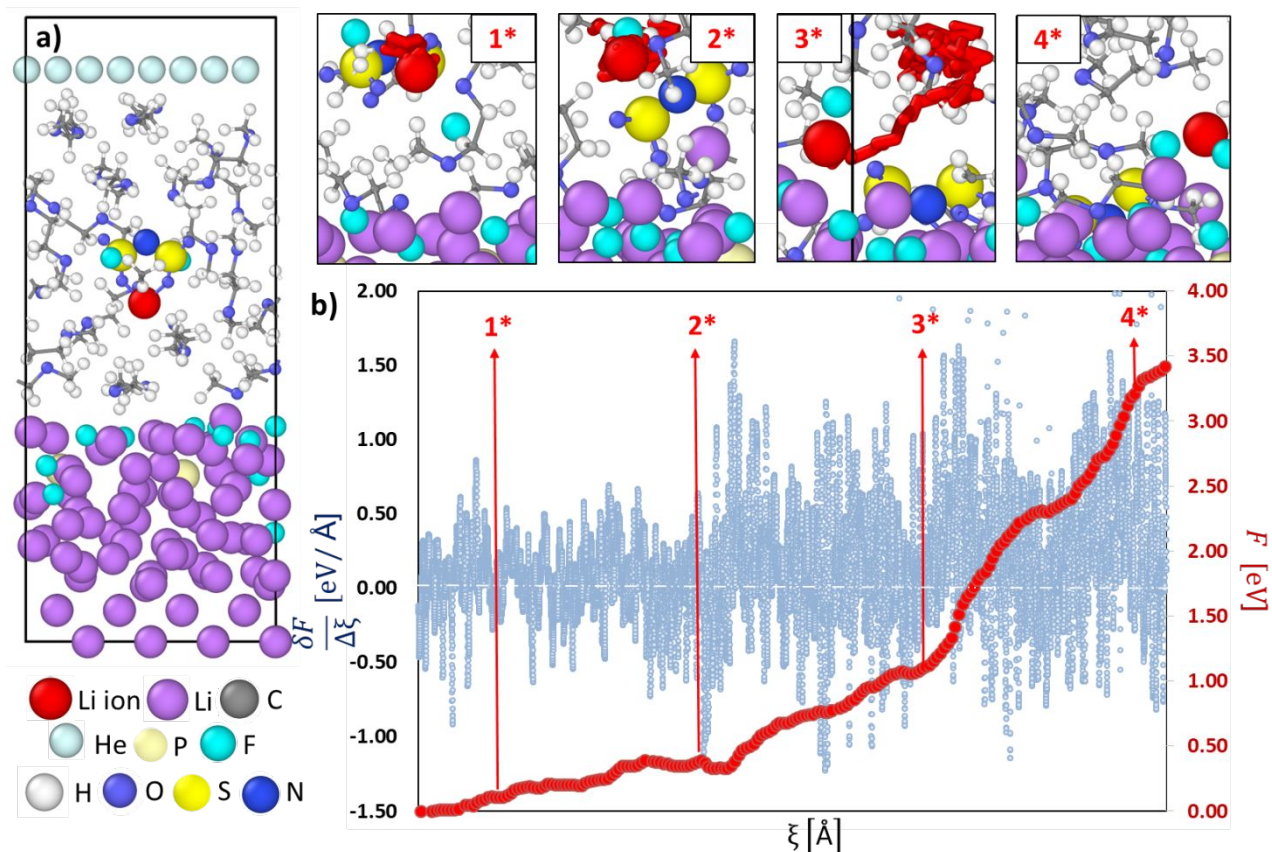


**Figure 12.** Free-energy profile of lithium cation deposition in presence of a nucleating SEI. a) Initial structure. b) Free energy profile, snapshots (images 1\* through 4\*) of the lithium cation diffusion pathway (illustrated by the red line) and deposition.

The initial energy barrier (Figure 12a  $\rightarrow$  1\*)  $\sim 0.11$  eV is the partial defluorination of the salt. The rotation of the salt fragment, leading to the defluorinated anion becoming close to the interphase is the following step (1\*  $\rightarrow$  2\*) having a barrier of  $\sim 0.28$  eV. Also, the lithium cation forms a LiF molecule with one of the fluorine atoms in the anion. The complete reduction of the partially defluorinated FSI anion is the following step (2\*  $\rightarrow$  3\*)

~0.68 eV, the new molecule of LiF formed by the lithium cation (red atom in Figure 12) and a F<sup>-</sup> remains solvated but close to the surface. This molecule becomes part of the model SEI locating on top of the nucleating LiF layer. The initial stages of nucleation of such layer in various electrolytes were recently discussed.<sup>60</sup> This stage has an energy barrier (3\* → 4\*) of ~2.21 eV, that corresponds to the diffusion of the reduction products of the salt toward the surface. It is possible that the diffusion of the Li cation from the top of the SEI to the SEI/anode interface where presumably the cation would be reduced may be done by ion knock-off mechanism through the SEI layer. This step is not studied here. We are currently analyzing this phenomenon with classical molecular dynamics simulations.

**Table 2.** Summary of Li ion motion from the electrolyte to the surface in various systems

System	Step	Main events	Barrier
LiPF <sub>6</sub> in DME: In the initial configuration anion and cation are separated	1* → 2*	stabilization of the cation (LiO → Li(O <sub>3</sub> ))	energy decreases, no barrier
	2* → 3*	desolvation from LiO <sub>3</sub>	0.24 eV
LiFSI in DME: In the initial configuration anion and cation are paired	1* → 2*	solvent tries to separate ion pair	0.7 eV
	2* → 3*	anion reduces, ion pair diffusion	0.53 eV

	$3^* \rightarrow 4^*$	anion completes reduction, cation deposits on surface	0.98 eV
LiFSI/DME/TFEO	Initial $\rightarrow 1^*$	anion-cation separation	2.95 eV
	$1^* \rightarrow 2^*$	diffusion of cation	1.41 eV
LiFSI/DME in presence of LiF thin film	Initial $\rightarrow 1^*$	partial defluorination of the anion	0.11 eV
	$1^* \rightarrow 2^*$	rotation of salt fragment;	0.28 eV
	$2^* \rightarrow 3^*$	further reduction of anion	0.68 eV
	$3^* \rightarrow 4^*$	integration of the new LiF to the nucleating film	2.21 eV

Table 2 summarizes the cation diffusion through different electrolytes. It is concluded that DME solvation does not impose a large energy penalty to the cation diffusion. Large barriers are found in presence of anion decomposition, because of the formation of negatively charged species that tend to retain the cation in solution. In addition, it is clear that breaking the ion-pair represents a high energetic cost, that may diminish as the ion pair moves to the surface where the anion usually reduces first.

Tuning the electrolyte is one of the ideas that are being used to modulate Li reactivity and induce smoother deposition. This is because the electrodeposition of the  $\text{Li}^+$  ions is highly influenced by the solvation shells that are formed by electrolyte components like salts, solvents, or additives. Figure 7 illustrates that DME with 1M salt concentration favors a relatively easy deposition of the cation with the solvent remaining stable. Yet, increasing salt concentration or using a diluent, as in localized high concentration electrolytes, can induce higher barriers for cation-anion separation in the electrolyte phase (as shown in relation to Figure 11), and perhaps a more controlled ionic deposition if the complex arrives near the surface before dissociation. This idea however requires further work and will be addressed in future reports.

Battery operating conditions may affect the  $\text{Li}^+$  electrodeposition kinetics and also they may alter energy barriers for each process of desolvation, diffusion, and deposition. Researchers have focused on the effect of the temperature on these barriers, an increase in temperature promotes transport of  $\text{Li}^+$  ions and self-diffusion of Li atoms on the surface by enabling them to overcome energy barriers.<sup>66</sup> However, temperature increases may not be always beneficial, and some of them could exacerbate the growth of dendrites.<sup>67</sup> All our simulations were run at 330K and we do not have currently a reference temperature for comparison of the calculated barriers. Further work may explore this point.

Another interesting question is how the nature of the electrode affects cation deposition. Previous studies investigated the mechanisms of cation deposition on metallic surfaces like Cu for different electrolytes.<sup>68</sup> It was found that cation deposition occurs in a two-step mechanism, the first step is driven by kinetics in solution, in a similar form as the

conclusions from this study. Thus, sufficiently far from the electrode, the ion solvation shell would behave similarly because diffusion through the bulk electrolyte should not change much even with structural and electronic differences in the electrode surface. However, in regions closer to the electrode surface, the second step involving the desolvation and deposition barriers will be affected. For example, surface polarization orbitals developed on the Cu surface<sup>68</sup> under an applied field, are much less significant than those on a Li surface. Thus, the Li surface favors cation deposition compared to Cu, although at the cost of surface stability.

## Conclusions

In this paper, we studied the lithium cation diffusion pathway as well as its deposition in several environments. Variations in the electrolyte included changes in the chemistry and structure of solvents and salts as well as the use of diluents or nucleating SEI. The solvation shell created around lithium cation has a great influence on the ability of the cation to diffuse as well as the electron environment that surrounds it. Whenever the  $\text{Li}^+$  is solvated by DME, the cation can be reduced by the lithium metal slab, the electrons are transferred from the bottom layers to the surface of the slab and then transferred to the lithium cation that is reduced. However, if the solvent used is EC-based the strong solvation shell and its electron affinity will prompt the reduction of the EC molecules instead of  $\text{Li}^+$ . If the solvation shell is difficult to break due to higher salt concentration or closer anion-cation interaction, the mobility of the cation is limited and its deposition is shown to be difficult.

It is important to remark that this study does not include any applied field. All the events are originated by molecular interactions and electron transfer due to differences in

electron affinities under the fields created by the molecules in the system. This corresponds to the real situation where a spontaneous SEI is formed by putting in contact a Li metal surface and an electrolyte solution.<sup>60</sup> In recent work, we have examined the effect of applied external fields and that of a simulation cell operating at constant electrode potential for cation electrodeposition on a Cu surface.<sup>68</sup> We showed that the effect an external field is necessary to obtain the reduction of the Li cation on the Cu surface. In this work we have illustrated the important effect of the electrolyte on facilitating or impeding such reduction on a Li surface, and the specific barriers that the ion would encounter in their way to the surface under various electrolyte solutions.

The slow growth approach allowed us to study the free energy diffusion pathway and deposition of the cation under specified collective variables leading it to leave its initial solvation shell and reaching the Li metal surface. Therefore, the energetic barriers for desolvation, diffusion and deposition were characterized. Although a lot of additional work is needed to achieve a comprehensive picture, this work provides new information on the initial cation deposition that we expect to guide additional experiments and simulations in an effort to achieving a better understanding of the initial stages of Li metal nucleation. Further directions will combine these insights with other models able to represent the statistical nature of deposition processes.

### **Conflicts of interest**

There are no conflicts of interest to declare.

### **Acknowledgements**

This work was supported by the U.S. Department of Energy's Office of Energy Efficiency and Renewable Energy (EERE), as part of the Battery 500 Consortium, Award Number DE-EE0008210. Supercomputer resources from the Texas A&M University High Performance Computer Center and from Texas Advanced Computing Center (TACC) are gratefully acknowledged.

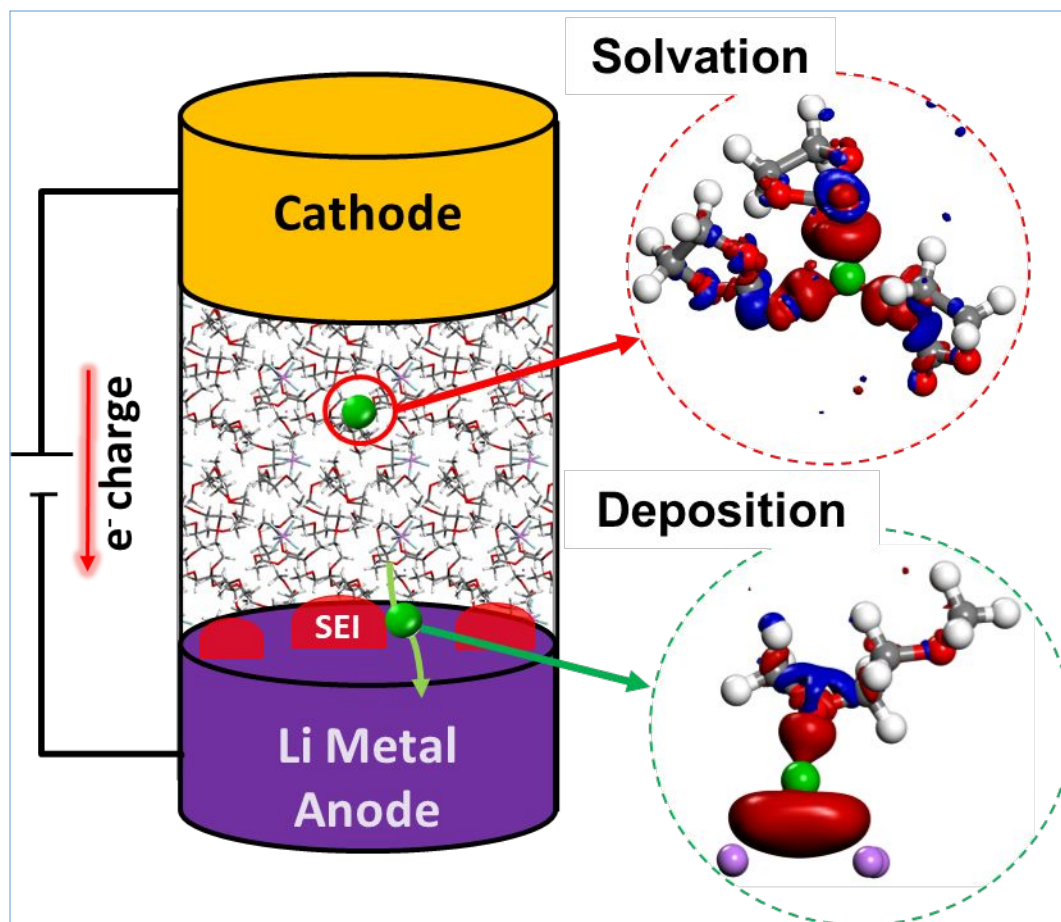
## References

- (1) Fang, C.; Wang, X.; Meng, Y. S. Key Issues Hindering a Practical Lithium-Metal Anode. *Trends in Chemistry* **2019**, *1*, 152-158.
- (2) Goodenough, J. B.; Kim, Y. Challenges for Rechargeable Li Batteries. *Chemistry of Materials* **2010**, *22*, 587-603.
- (3) Chen, X.; Hou, T.; Persson, K. A.; Zhang, Q. Combining theory and experiment in lithium-sulfur batteries: Current progress and future perspectives. *Materials Today* **2019**, *22*, 142-158.
- (4) Fu, K.; Gong, Y.; Hitz, G. T.; McOwen, D. W.; Li, Y.; Xu, S.; Wen, Y.; Zhang, L.; Wang, C.; Pastel, G.; Dai, J.; Liu, B.; Xie, H.; Yao, Y.; Wachsman, E. D.; Hu, L. Three-dimensional bilayer garnet solid electrolyte based high energy density lithium metal-sulfur batteries. *Energy & Environmental Science* **2017**, *10*, 1568-1575.
- (5) Lai, J.; Xing, Y.; Chen, N.; Li, L.; Wu, F.; Chen, R. Electrolytes for Rechargeable Lithium-Air Batteries. *Angewandte Chemie International Edition* **2020**, *59*, 2974-2997.
- (6) Lin, D.; Liu, Y.; Cui, Y. Reviving the lithium metal anode for high-energy batteries. *Nature Nanotechnology* **2017**, *12*, 194.
- (7) Fan, L.; Zhuang, H. L.; Zhang, W.; Fu, Y.; Liao, Z.; Lu, Y. Stable Lithium Electrodeposition at Ultra-High Current Densities Enabled by 3D PMF/Li Composite Anode. *Advanced Energy Materials* **2018**, *8*, 1703360.
- (8) Fan, L.; Zhuang, H. L.; Gao, L.; Lu, Y.; Archer, L. A. Regulating Li deposition at artificial solid electrolyte interphases. *Journal of Materials Chemistry A* **2017**, *5*, 3483-3492.
- (9) Tripathi, A. M.; Su, W.-N.; Hwang, B. J. In situ analytical techniques for battery interface analysis. *Chemical Society Reviews* **2018**, *47*, 736-851.
- (10) Harry, K. J.; Hallinan, D. T.; Parkinson, D. Y.; MacDowell, A. A.; Balsara, N. P. Detection of subsurface structures underneath dendrites formed on cycled lithium metal electrodes. *Nature Materials* **2013**, *13*, 69.
- (11) Xu, X.; Wang, S.; Wang, H.; Hu, C.; Jin, Y.; Liu, J.; Yan, H. Recent progresses in the suppression method based on the growth mechanism of lithium dendrite. *Journal of Energy Chemistry* **2018**, *27*, 513-527.
- (12) Liu, J.; Bao, Z.; Cui, Y.; Dufek, E. J.; Goodenough, J. B.; Khalifah, P.; Li, Q.; Liaw, B. Y.; Liu, P.; Manthiram, A.; Meng, Y. S.; Subramanian, V. R.; Toney, M. F.; Viswanathan, V. V.; Whittingham, M. S.; Xiao, J.; Xu, W.; Yang, J.; Yang, X.-Q.; Zhang, J.-G. Pathways for practical high-energy long-cycling lithium metal batteries. *Nature Energy* **2019**, *4*, 180-186.

- (13) Qian, J.; Henderson, W. A.; Xu, W.; Bhattacharya, P.; Engelhard, M.; Borodin, O.; Zhang, J.-G. High rate and stable cycling of lithium metal anode. *Nature Communications* **2015**, *6*, 6362.
- (14) Zheng, G.; Lee, S. W.; Liang, Z.; Lee, H.-W.; Yan, K.; Yao, H.; Wang, H.; Li, W.; Chu, S.; Cui, Y. Interconnected hollow carbon nanospheres for stable lithium metal anodes. *Nature Nanotechnology* **2014**, *9*, 618-623.
- (15) Xu, X.; Wang, S.; Wang, H.; Xu, B.; Hu, C.; Jin, Y.; Liu, J.; Yan, H. The suppression of lithium dendrite growth in lithium sulfur batteries: A review. *Journal of Energy Storage* **2017**, *13*, 387-400.
- (16) Yamada, Y.; Furukawa, K.; Sodeyama, K.; Kikuchi, K.; Yaegashi, M.; Tateyama, Y.; Yamada, A. Unusual Stability of Acetonitrile-Based Superconcentrated Electrolytes for Fast-Charging Lithium-Ion Batteries. *Journal of the American Chemical Society* **2014**, *136*, 5039-5046.
- (17) Li, L.; Basu, S.; Wang, Y.; Chen, Z.; Hundekar, P.; Wang, B.; Shi, J.; Shi, Y.; Narayanan, S.; Koratkar, N. Self-heating-induced healing of lithium dendrites. *Science* **2018**, *359*, 1513.
- (18) Wang, J.; Huang, W.; Pei, A.; Li, Y.; Shi, F.; Yu, X.; Cui, Y. Improving cyclability of Li metal batteries at elevated temperatures and its origin revealed by cryo-electron microscopy. *Nature Energy* **2019**, *4*, 664-670.
- (19) Vishnugopi, B. S.; Hao, F.; Verma, A.; Mukherjee, P. P. Double-Edged Effect of Temperature on Lithium Dendrites. *ACS Applied Materials & Interfaces* **2020**, *12*, 23931-23938.
- (20) Vishnugopi, B. S.; Hao, F.; Verma, A.; Mukherjee, P. P. Surface diffusion manifestation in electrodeposition of metal anodes. *Physical Chemistry Chemical Physics* **2020**, *22*, 11286-11295.
- (21) Jäckle, M.; Helmbrecht, K.; Smits, M.; Stottmeister, D.; Groß, A. Self-diffusion barriers: possible descriptors for dendrite growth in batteries? *Energy & Environmental Science* **2018**, *11*, 3400-3407.
- (22) Barton, J. L.; Bockris, J. O.; apos; m; Ubbelohde, A. R. J. P. The electrolytic growth of dendrites from ionic solutions. *Proceedings of the Royal Society of London. Series A. Mathematical and Physical Sciences* **1962**, *268*, 485-505.
- (23) Witten, T. A.; Sander, L. M. Diffusion-Limited Aggregation, a Kinetic Critical Phenomenon. *Physical Review Letters* **1981**, *47*, 1400-1403.
- (24) Chazalviel, J. N. Electrochemical aspects of the generation of ramified metallic electrodeposits. *Physical Review A* **1990**, *42*, 7355-7367.
- (25) Yamaki, J.-i.; Tobishima, S.-i.; Hayashi, K.; Keiichi, S.; Nemoto, Y.; Arakawa, M. A consideration of the morphology of electrochemically deposited lithium in an organic electrolyte. *Journal of Power Sources* **1998**, *74*, 219-227.
- (26) Li, Z.; Huang, J.; Yann Liaw, B.; Metzler, V.; Zhang, J. A review of lithium deposition in lithium-ion and lithium metal secondary batteries. *Journal of Power Sources* **2014**, *254*, 168-182.
- (27) Kamphaus, E. P.; Hight, K.; Dermott, M.; Balbuena, P. B. Model systems for screening and investigation of lithium metal electrode chemistry and dendrite formation. *Physical Chemistry Chemical Physics* **2020**, *22*, 575-588.
- (28) Hao, F.; Verma, A.; Mukherjee, P. P. Mesoscale Complexations in Lithium Electrodeposition. *ACS Applied Materials & Interfaces* **2018**, *10*, 26320-26327.
- (29) Jana, A.; Woo, S. I.; Vikrant, K. S. N.; García, R. E. Electrochemomechanics of lithium dendrite growth. *Energy & Environmental Science* **2019**, *12*, 3595-3607.
- (30) Cheng, X.-B.; Zhang, R.; Zhao, C.-Z.; Zhang, Q. Toward Safe Lithium Metal Anode in Rechargeable Batteries: A Review. *Chemical Reviews* **2017**, *117*, 10403-10473.
- (31) Bucko, T. Ab initio calculations of free-energy reaction barriers. *Journal of Physics: Condensed Matter* **2008**, *20*, 064211.

- (32) Ciccotti, G.; Ferrario, M. Blue Moon Approach to Rare Events. *Molecular Simulation* **2004**, *30*, 787-793.
- (33) Kresse, G.; Furthmüller, J. Efficiency of ab-initio total energy calculations for metals and semiconductors using a plane-wave basis set. *Computational Materials Science* **1996**, *6*, 15-50.
- (34) Kresse, G.; Hafner, J. Ab initio molecular dynamics for liquid metals. *Physical Review B* **1993**, *47*, 558.
- (35) Kresse, G.; Hafner, J. Ab initio molecular-dynamics simulation of the liquid-metal-amorphous-semiconductor transition in germanium. *Physical Review B* **1994**, *49*, 14251-14269.
- (36) Blöchl, P. E. Projector augmented-wave method. *Physical review B* **1994**, *50*, 17953.
- (37) Kresse, G.; Joubert, D. From ultrasoft pseudopotentials to the projector augmented-wave method. *Physical Review B* **1999**, *59*, 1758-1775.
- (38) Perdew, J. P.; Burke, K.; Ernzerhof, M. Generalized Gradient Approximation Made Simple. *Physical Review Letters* **1996**, *77*, 3865-3868.
- (39) Monkhorst, H. J.; Pack, J. D. Special points for Brillouin-zone integrations. *Physical Review B* **1976**, *13*, 5188-5192.
- (40) Camacho-Forero, L. E.; Smith, T. W.; Bertolini, S.; Balbuena, P. B. Reactivity at the Lithium-Metal Anode Surface of Lithium-Sulfur Batteries. *J. Phys. Chem. C* **2015**, *119*, 26828-26839.
- (41) Maple, J. R.; Dinur, U.; Hagler, A. T. DERIVATION OF FORCE-FIELDS FOR MOLECULAR MECHANICS AND DYNAMICS FROM ABINITIO ENERGY SURFACES. *Proc. Natl. Acad. Sci. U. S. A.* **1988**, *85*, 5350-5354.
- (42) Nosé, S. A unified formulation of the constant temperature molecular dynamics methods. **1984**, *81*, 511-519.
- (43) Hoover, W. G. Canonical dynamics: Equilibrium phase-space distributions. *Physical Review A* **1985**, *31*, 1695-1697.
- (44) Tang, W.; Sanville, E.; Henkelman, G. A grid-based Bader analysis algorithm without lattice bias. *Journal of Physics: Condensed Matter* **2009**, *21*, 084204.
- (45) Henkelman, G.; Arnaldsson, A.; Jónsson, H. A fast and robust algorithm for Bader decomposition of charge density. *Computational Materials Science* **2006**, *36*, 354-360.
- (46) Leung, K. First-Principles Modeling of Mn(II) Migration above and Dissolution from LixMn2O4 (001) Surfaces. *Chemistry of Materials* **2017**, *29*, 2550-2562.
- (47) Klyukin, K.; Zagalskaya, A.; Alexandrov, V. Role of Dissolution Intermediates in Promoting Oxygen Evolution Reaction at RuO2(110) Surface. *The Journal of Physical Chemistry C* **2019**, *123*, 22151-22157.
- (48) Klyukin, K.; Rosso, K. M.; Alexandrov, V. Iron Dissolution from Goethite ( $\alpha$ -FeOOH) Surfaces in Water by Ab Initio Enhanced Free-Energy Simulations. *The Journal of Physical Chemistry C* **2018**, *122*, 16086-16091.
- (49) Benedek, R. Role of Disproportionation in the Dissolution of Mn from Lithium Manganate Spinel. *The Journal of Physical Chemistry C* **2017**, *121*, 22049-22053.
- (50) Komeiji, Y. Implementation of the blue moon ensemble method. *Chem-bio Informatics Journal* **2007**, *7*, 12-23.
- (51) Cheng, T.; Xiao, H.; Goddard, W. A. Free-Energy Barriers and Reaction Mechanisms for the Electrochemical Reduction of CO on the Cu(100) Surface, Including Multiple Layers of Explicit Solvent at pH 0. *The Journal of Physical Chemistry Letters* **2015**, *6*, 4767-4773.
- (52) Qin, X. P.; Shao, M. H.; Balbuena, P. B. Elucidating mechanisms of Li plating on Li anodes of lithium-based batteries. *Electrochim. Acta* **2018**, *284*, 485-494.
- (53) Jensen, F.: *Introduction to Computational Chemistry*; Wiley, 2016.

- (54) Wang, Y.; Nakamura, S.; Ue, M.; Balbuena, P. B. Theoretical studies to understand surface chemistry on carbon anodes for lithium-ion batteries: Reduction mechanisms of ethylene carbonate. *J. Am. Chem. Soc.* **2001**, *123*, 11708-11718.
- (55) Xing, L.; Zheng, X.; Schroeder, M.; Alvarado, J.; von Wald Cresce, A.; Xu, K.; Li, Q.; Li, W. Deciphering the Ethylene Carbonate–Propylene Carbonate Mystery in Li-Ion Batteries. *Accounts of Chemical Research* **2018**, *51*, 282-289.
- (56) Han, S. Structure and dynamics in the lithium solvation shell of nonaqueous electrolytes. *Scientific Reports* **2019**, *9*, 5555.
- (57) Kamphaus, E. P.; Balbuena, P. B. First-Principles Investigation of Lithium Polysulfide Structure and Behavior in Solution. *Journal of Physical Chemistry C* **2017**, *121*, 21105-21117.
- (58) Xu, K.; Lam, Y.; Zhang, S. S.; Jow, T. R.; Curtis, T. B. Solvation Sheath of Li<sup>+</sup> in Nonaqueous Electrolytes and Its Implication of Graphite/Electrolyte Interface Chemistry. *The Journal of Physical Chemistry C* **2007**, *111*, 7411-7421.
- (59) Xu, K. “Charge-transfer” process at graphite/electrolyte interface and the solvation sheath structure of Li<sup>+</sup> in nonaqueous electrolytes. *Journal of The Electrochemical Society* **2007**, *154*, A162-A167.
- (60) Ospina Acevedo, F.; Guo, N.; Balbuena, P. B. Lithium Oxidation and Electrolyte Decomposition at Li-Metal/Liquid Electrolyte Interfaces. *Journal of Materials Chemistry A* **2020**, *8*, 17036-17055.
- (61) Perez Beltran, S.; Cao, X.; Zhang, J.-G.; Balbuena, P. B. Localized High Concentration Electrolytes for High Voltage Lithium–Metal Batteries: Correlation between the Electrolyte Composition and Its Reductive/Oxidative Stability. *Chemistry of Materials* **2020**, *32*, 5973-5984.
- (62) Pranay Reddy, K.; Fischer, P.; Marinaro, M.; Wohlfahrt-Mehrens, M. J. C. Improved Li–Metal Cycling Performance in High Concentrated Electrolytes for Li-O<sub>2</sub> Batteries. *ChemElectroChem* **2018**, *5*, 2758-2766.
- (63) Zheng, J.; Lochala, J. A.; Kwok, A.; Deng, Z. D.; Xiao, J. Research Progress towards Understanding the Unique Interfaces between Concentrated Electrolytes and Electrodes for Energy Storage Applications. *Advanced Science* **2017**, *4*, 1700032.
- (64) Zheng, Y.; Soto, F. A.; Ponce, V.; Seminario, J. M.; Cao, X.; Zhang, J.-G.; Balbuena, P. B. Localized high concentration electrolyte behavior near a lithium–metal anode surface. *Journal of Materials Chemistry A* **2019**, *7*, 25047-25055.
- (65) Cao, X.; Ren, X.; Zou, L.; Engelhard, M. H.; Huang, W.; Wang, H.; Matthews, B. E.; Lee, H.; Niu, C.; Arey, B. W.; Cui, Y.; Wang, C.; Xiao, J.; Liu, J.; Xu, W.; Zhang, J.-G. Monolithic solid–electrolyte interphases formed in fluorinated orthoformate-based electrolytes minimize Li depletion and pulverization. *Nature Energy* **2019**, *4*, 796-805.
- (66) Aryanfar, A.; Cheng, T.; Colussi, A. J.; Merinov, B. V.; Goddard, W. A.; Hoffmann, M. R. Annealing kinetics of electrodeposited lithium dendrites. *The Journal of Chemical Physics* **2015**, *143*, 134701.
- (67) Zhu, Y.; Xie, J.; Pei, A.; Liu, B.; Wu, Y.; Lin, D.; Li, J.; Wang, H.; Chen, H.; Xu, J.; Yang, A.; Wu, C.-L.; Wang, H.; Chen, W.; Cui, Y. Fast lithium growth and short circuit induced by localized-temperature hotspots in lithium batteries. *Nature Communications* **2019**, *10*, 2067.
- (68) Longo, R. C.; Camacho-Forero, L. E.; Balbuena, P. B. Charge-mediated cation deposition on metallic surfaces. *Journal of Materials Chemistry A* **2019**, *7*, 8527-8539.



Barriers for desolvation, diffusion through electrolyte, and reduction on metal surface and electrolyte effects are evaluated